Bull Earthquake Eng (2015) 13:1587–1612
DOI 10.1007/s10518-014-9685-y

ORIGINAL RESEARCH PAPER

Updated predictive equations for broadband (0.01–10 s) horizontal response spectra and peak ground motions, based on a global dataset of digital acceleration records

Carlo Cauzzi · Ezio Faccioli · Manuela Vanini · Aldo Bianchini

Received: 4 June 2014 / Accepted: 25 September 2014 / Published online: 9 October 2014

Abstract Presented herein is an updated model for empirical prediction of 5 %-damped elastic response spectra in the period range 0–10 s, peak ground acceleration and velocity, based on a global dataset of digital acceleration records. The predictive model features saturation of the shaking parameters with both magnitude M_W and distance R_{RUP}, magnitude-dependent distance attenuation, alternative parameterisations of the amplification effects due to local site conditions (based either on ground types or $V_{S,30}$) and corrective terms for style-of-faulting. The calibration dataset comprises more than $1{,}880 \times 2$ orthogonal horizontal accelerometer records with $R_{RUP} < 150$ km from 98 global earthquakes with $4.5 \leq M_W \leq 7.9$. The processing technique applied to the acceleration data optimises the reliability of the predictions at long periods, as required by displacement-based design techniques. Developed independently of the recent *NGA-West2* and *RESORCE*-based models, the new predictive tool effectively contributes to capturing the epistemic uncertainties associated with the prediction of seismic shaking levels for engineering applications.

Keywords GMPE · Response spectra · Long periods · Site effects

Electronic supplementary material The online version of this article (doi:10.1007/s10518-014-9685-y) contains supplementary material, which is available to authorized users.

C. Cauzzi (✉)
Swiss Seismological Service, ETH Zurich, Sonneggstrasse 5, 8092 Zurich, Switzerland
e-mail: carlo.cauzzi@sed.ethz.ch

E. Faccioli · M. Vanini
Department of Civil and Environmental Engineering, Politecnico di Milano, Piazza L. da Vinci, 32, 20133 Milan, Italy

A. Bianchini
Via dei Vitelli 3, 06012 Città di Castello, Italy

1 Introduction and motivation

The last year witnessed two significant events in the very active domain of empirical models for prediction of ground-motions and response spectra, i.e. the publication of two new sets of ground-motion prediction equations (GMPEs), stemming from the release of two large databases of accelerometer records. These are *NGA-West2*, a global dataset compiled in California (Ancheta et al. 2014) as a result of enlarging and updating the earlier *NGA-West1* (just *NGA* in the following) database, and *RESORCE*, a reference database which contains seismic ground-motions, response spectra and associated metadata from Europe and the Middle East (Akkar et al. 2014a) and whose compilation has similarities to the earlier *NGA* database. Comparative aspects of the *RESORCE* and *NGA* datasets and, in part, of the GMPEs derived so far from them are discussed in Douglas et al. (2014).

Amongst the predictive tools derived from *NGA-West2* is that proposed by Boore et al. (2014), for which the authors state that they "sought simple functions for our GMPEs, with the smallest number of predictor variables required to provide a reasonable fit to the data". The predictor variables are indeed the standard ones used in this domain—moment magnitude M_W, Joyner and Boore (1981) distance R_{JB}, $V_{S,30}$ for site characterisation and style-of-faulting—but it may be noted that the GMPEs in question make use of 11 regression-determined coefficients for magnitude scaling and path dependence (base case), 4 regression-determined site coefficients (base case), and 8 coefficients for describing the aleatory uncertainty, for a total of 23 independent parameters. It is thus understandable that not all the terms in these GMPEs are susceptible of a physical interpretation, as for instance is the case with the combined meaning of the three magnitude scaling coefficients at magnitudes less than the "hinge" magnitude value. More difficult to understand in the light of basic physical evidence is that the total standard deviation σ, strongly dependent on magnitude (i.e. heteroschedastic), exhibits an increasing trend with respect to period, from 0 to 10 s, due to the variation of the within-event component ϕ. In fact, simple empirical attenuation models based exclusively on digital recordings tend to show the opposite (see e.g. Cauzzi and Faccioli 2008), consistent with the fact that path irregularity and site effects on variability of ground motion should tend to smooth out at long period. While the feature of a clear physical interpretation is not an indispensable attribute for the coefficients of an empirical model, it is often useful in applications, e.g. in interpreting results of probabilistic seismic hazard assessment (PSHA).

The set of "European" GMPEs developed from the common *RESORCE* database, was recently published in a special issue of the Bulletin of Earthquake Engineering (January 2014) and reviewed in detail by Douglas et al. (2014). All these attenuation models feature total standard deviations σ between 0.3 and 0.4 in log_{10} units in the considered period range from 0 to 4 s, exhibiting also in this case an overall, moderately increasing trend with period. Bindi et al. (2014) argued that this behaviour might be due to "the reduction in the number of the considered recordings at long period and to the processing scheme which was not optimized for long periods". The first explanation implies that the sample size (i.e. the number of data points) available at long periods is insufficient to correctly estimate the population SD.

The models in question, some of which are non-parametric, predict quite similar response spectra on rock-like ground types ($V_{S,30} \sim 800\,\mathrm{m\,s^{-1}}$), in the magnitude and distance range where the predictions are best constrained by the data, i.e. for $M_W = 5$–7 and $10 < R_{JB} < 100$ km (see e.g. Bindi et al. 2014, top panels of their Fig. 1). However, due to the combined effect of the differences resulting from varying data selection criteria and derivation techniques, they "demonstrate that epistemic uncertainty in ground-motion prediction in Europe and the Middle East remains large and it cannot be explained by differences

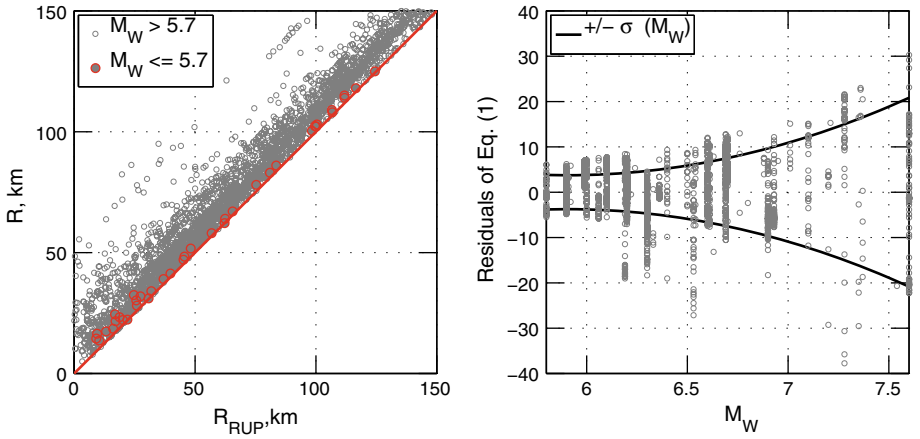

Fig. 1 *LHS* $R_{RUP}-R-M_W$ dataset used for estimating the coefficients of Eq. (1). The *red straight line* is the bisector of the $R_{RUP}-R$ plane. Note the distribution of data with $M_W < 5.7$, for which the hypothesis $R = R_{RUP}$ could not be rejected. *RHS* Residuals of Eq. (1) as a function of magnitude. The *black curves* represent the SD model of Eq. (1), described in the text

in the metadata of the strong-motion records used or different sets of independent parameters" (Douglas et al. 2014). One aspect that may deserve further evaluation is the influence of low-pass filtering on the reliability of the long period ($T > 1$ s) spectrum ordinates by the GMPEs derived from the *RESORCE* database, as it will be shown in a later section herein. A typical parametric model of this set (Bindi et al. 2014) is significantly less complex than the previously mentioned one of Boore et al. (2014), as it makes use of 15 regression coefficients plus three auxiliary ones.

The foregoing models of both groups are the state-of-the-art in response spectral acceleration prediction in the global and European contexts, and provide a solid basis for quantifying epistemic uncertainty in such prediction. One may, however, legitimately ask whether predictions of comparable quality could not be derived with alternative (possibly simpler) models, using different (possibly global and entirely digital) datasets and processing, and a different (though state-of-the-art) regression technique. Such a derivation is the goal in this study, which continues and updates the work initiated more than 5 years ago with a simple model for predicting displacement spectral response ordinates *DRS* (Cauzzi and Faccioli 2008) based, to our knowledge for the first time, on an entirely digital database that allowed to reliably predict spectral ordinates up to long vibration periods $T > 10$ s. That model was subsequently selected in the *SHARE* (http://www.share-eu.org/) project among the predictive tools for SHA in the greater European region (Delavaud et al. 2012), and underwent a few modifications in subsequent versions presented only at international conferences and workshops. Cauzzi (2008) enlarged the reference dataset with digital data for $4.5 \leq M_W \leq 5.0$ to test the sensitivity of the median *DRS* predictions to the lower magnitude bound of the reference dataset. Cauzzi et al. (2008) extended the upper magnitude bound to 7.6 and used the finite-fault distance metric R_{RUP} (the closest distance between the recording station and the ruptured fault) as a predictor for a subset of the earthquakes in their databank. Faccioli et al. (2010a) extended the dataset with additional records aimed at filling some apparent gaps in the magnitude and distance distribution of the data, increased the quality of metadata of the previous datasets, and proposed predictive equations for $T > 1$ s and M_W in the range 4.5–7.6, whilst introducing a distance term also dependent on magnitude (similar to Fukushima and Tanaka 1990; Kanno 2006). Cauzzi et al. (2011) proposed a model for

prediction of *DRS* ($T > 1\,s$) and $R_{RUP} < 150$ km based on worldwide recorded earthquakes with $3 < M_W < 8$, with a large contribution of the Swiss digital dataset for $M_W < 4.5$ and exploring the use of $V_{S,QWL}$ (Joyner et al. 1981), the quarter–wavelet velocity approximation, as a predictor. As mentioned, however, a comprehensive update of the original Cauzzi and Faccioli (2008) model has never been published in the international peer-reviewed literature and this is therefore the objective of the present article, which summarises several years of our research work on the topic.

Focusing on the moment magnitude range 4.5–8 of primary interest for engineering applications, we selectively document herein both the strengthening of the database used and illustrate in greater detail the modifications just mentioned. We then derive an updated set of predictive equations for horizontal 5 %-damped elastic response spectra, peak-ground velocity and peak ground acceleration, with emphasis placed on the site amplification effects on ground-motion and the response spectra predictions. Our results are compared with a selection of those recently published, based on *NGA-West2* and *RESORCE*.

A final note on terminology: we try to avoid as much as possible the abuse of the acronym GMPE when referring to our empirical prediction model for response spectra as, formally speaking, in spite of their well-known asymptotic properties, earthquake response spectra are not ground motions.

2 Dataset of acceleration records

As mentioned in the previous section, the first finite-fault-based update of the original Cauzzi and Faccioli (2008) predictions was that of Cauzzi et al. (2008), who extended the maximum magnitude to 7.6 and calculated the rupture distance for some of the records in the database. Due to the small number of data with calculated rupture distance, however, the model proposed by Cauzzi et al. (2008) showed some irregularities in the pattern of spectra in the critical cases of high magnitude and short distance. To overcome this problem we started from late 2008 to increase the number of records with associated rupture distance R_{RUP} in the dataset by searching for fault models both in the published literature and on the websites of authoritative seismological Institutions. We complemented this compilation effort with the data available in the *NGA* database to develop a simple conversion equation between focal distance R and R_{RUP} given by:

$$R = 1.38 + R_{RUP} + 0.0145e^{M_W} + \sigma(M_W) \tag{1}$$

Equation (1) was developed based on ~2,870 distance pairs in the range $5.5 \leq M_W \leq 7.6$ and with $R_{RUP} \leq 150$ km, and supersedes the conversion equation suggested by Faccioli et al. (2010a). The dataset used to derive Eq. (1) is shown in Fig. 1 (LHS). Equation (1) means that the difference between the two distance measures increases with increasing magnitude, consistent with the increase of the characteristic dimensions of the fault with M_W. The functional form of Eq. (1) was pragmatically preferred to a set of linear relationships between R and R_{RUP}, initially derived segregating the available data into different magnitude bins. These preliminary investigations and the distribution of the residuals of Eq. (1) with respect to the predictors showed that the standard deviation of Eq. (1) is a function of M_W, reasonably modelled by the quadratic equation $\sigma = 209 - 69.6\,M_W + 5.9\,M_W^2$ (see Fig. 1, RHS). Based on the dataset used in the present study, only minor differences could be appreciated on average between R and R_{RUP} for events with $M_W < 6$. In particular, for $M_W < 5.7$ we could not reject the hypothesis that R_{RUP} is equivalent, at least in a statistical sense, to R (see Fig. 1, LHS). We therefore identified $M_W = 5.7$ as the threshold below which the differences

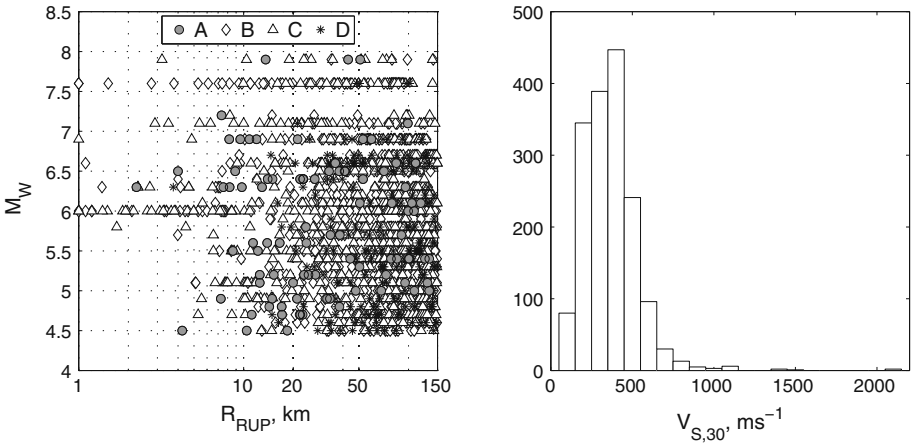

Fig. 2 *LHS* Moment magnitude M_W and rupture distance R_{RUP} distribution in the present dataset; data with $R_{RUP} < 1$ km are plotted at 1 km. *RHS* Hystogram of $V_{S,30}$ values in the present dataset

between the two measures are statistically insignificant. Hence, although in the subsequent updates of the database we decided to retain only records generated by events with known fault planes, we relaxed this requirement for the range $M_W \leq 5.7$, where the assumption $R_{RUP} \sim R$ could be made. Note that, based on Wells and Coppersmith (1994), the radius of the estimated rupture area (assuming a circular fault) of a $M_W = 5.7$ event would be <4 km, i.e. comparable with the uncertainty associated to focal depth determination in case of sparse network geometry or lack of refined velocity models (see e.g. Bormann 2012).

As a result of the successive updates, the database used in this study contains a total of ~1,880 × 2 orthogonal horizontal component records (the vertical records are also available but will be the subject of future investigations) generated from 98 global earthquakes with $4.5 \leq M_W \leq 7.9$. The focal depth of the events does not exceed 20 km. The dataset comprises 49 Japanese earthquakes, 35 events occurred in the Pan-European region, 7 earthquakes located in the Western US, 5 events from New Zealand and 2 from China and Taiwan. The distribution of magnitude, distance and ground types in the databank is shown in the LHS of Fig. 2, where a log scale is used for the x-axis to emphasise the distribution of data in the near-field. 7 % of the available data are recorded on Eurocode 8 (CEN 2004) ground type A, 43 % on type B, 40 % on type C and 10 % on type D sites. For a vast majority, namely 1,660 records, $V_{S,30}$ values are also available, as shown in the RHS panel of Fig. 2 and their mean value is equal to 365 m s^{-1}. Concerning the focal mechanism, defined according to Boore and Atkinson (2008), 20 earthquakes have normal faulting style, 26 have reverse faulting style and 43 are associated with strike-slip style-of-faulting. The list of the earthquakes used in this study is given in Table 1, along with basic information about epicentral region, depth, magnitude and style-of-faulting of each event. Table 2 lists details about the distribution of events and records by geographical origin, faulting style and magnitude. Data are segregated in different magnitude-distance bins in Table 3: in each bin, the number of records available for each EC8 ground type is given.

Following Paolucci et al. (2008) and Cauzzi and Faccioli (2008), we avoided filtering waveform data with a probability $P > 0.9$ of long-period disturbance levels being <15 %. Both horizontal components of the remaining data were high-pass filtered with a $T_c = 20$ s cut-off. The processing technique adopted herein is consistent with the performance evaluation of Cauzzi and Clinton (2013) of modern digital accelerometer stations.

Table 1 Earthquakes in the reference database

Earthquake date and time (UTC)	Epicentral area (country, number of records)	SOF	Depth (km)	M_W	Reference for fault plane solution or R_{RUP} values
1980_November_23_18:34	Irpinia (IT, 9)	N	16[a]	6.9[b,a]	Cauzzi et al. (2008)
1990_March_19_10:46	Reykjanes Peninsula (IC, 3)	SS	6[a]	4.7[a]	–[p]
1992_December_27_12:23	N of Hveragerdi (IC, 4)	SS	3[a]	4.8[a]	–
1995_January_16_20:46	Hyogo–Ken Nanbu (J, 4)	SS	17.9[c]	6.9[b]	Cauzzi et al. (2008)
1995_November_06_18:51	Kozani (aftershock) (GR, 4)	N	13[a]	4.8[a]	–
1996_August_10_23:10	Honshu (J, 27)	SS	10[d]	5.7[b]	–
1996_September_09_04:34	Kyushu (J, 10)	N	20[d]	5.7[b]	–
1997_March_04_03:51	Central Izu Peninsula (J, 24)	SS	2[d]	5.5[b]	Yoshida et al. (1999)
1997_March_26_08:31	NW Kagoshima Prefecture (J, 63)	SS	8[d]	6.1[b]	Horikawa (2001)
1997_April_02_19:33	NW Kagoshima Prefecture (J, 43)	SS	9[d]	5.4[b]	–
1997_April_10_16:13	Umbria Marche (aftershock) (IT, 3)	N	2[a]	4.7[a]	–
1997_August_24_03:04	Mt. Hengill Area (IC, 2)	SS	5[a]	4.9[a]	–
1997_May_10_07:57	Ardakul (I, 3)	SS	15[b]	7.2[b]	Ghasemi et al. (2008)
1997_May_13_05:38	NW Kagoshima Prefecture (J, 68)	SS	8[d]	6[b]	Horikawa (2001)
1997_June_25_09:50	Yamaguchi Prefecture (J, 38)	SS	12[d]	5.8[b]	Ide (1999)
1997_July_10_05:09	Umbria Marche (aftershock) (IT, 3)	N	3[a]	4.5[a]	–
1997_February_04_10:37	Garmkhan (I, 2)	SS	15[b]	6.5[b]	Ghasemi et al. (2008)
1997_September_11_19:07	Umbria–Marche (aftershock) (IT, 3)	N	2[a]	4.9[a]	–
1997_October_06_23:24	Umbria–Marche (IT, 2)	N	7[a]	5.5[b,a]	–
1997_October_12_11:08	Umbria–Marche (IT, 4)	N	6[a]	5.2[b,a]	–
1997_October_14_15:23	Umbria–Marche (IT, 4)	N	7[a]	5.6[a]	–
1998_April_03_07:26	Umbria–Marche (IT, 2)	N	6[a]	5.1[b,a]	–
1998_May_03_02:09	E Off Izu Peninsula (J, 23)	SS	3[d]	5.5[b]	–
1998_August_15_18:31	Hida Mountains (J, 38)	SS	5[d]	5.3[b]	–
1998_September_03_07:58	N Iwate Prefecture (J, 20)	R	10[d]	5.9[b]	Cauzzi et al. (2008)
1999_August_17_00:01	Izmit (T, 13)	SS	17[a]	7.6[b,a]	Cauzzi et al. (2008)
1999_August_19_15:17	Izmit (T, 1)	N	12[a]	5.1[b,a]	–
1999_August_31_08:10	Izmit (T, 9)	N	4[a]	5.2[a]	–
1999_September_20_17:47	ChiChi (TW, 79)	R	8[n]	7.6[b]	Cauzzi et al. (2008)
1999_October_16_09:46	Hector Mine (C, 19)	SS	15[b]	7.1[b]	Cauzzi et al. (2008)
1999_November_12_16:57	Duzce (T, 8)	SS	14[a]	7.2[a]	Cauzzi et al. (2008)
2000_June_17_15:40	South Iceland (IC, 10)	SS	15[b,a]	6.5[b,a]	Cauzzi et al. (2008)
2000_June_21_00:51	South Iceland (IC, 10)	SS	15[b,a]	6.4[b,a]	Cauzzi et al. (2008)
2000_June_29_06:30	Near Miyakejima Island (J, 8)	SS	20[d]	5.6[b]	–

Table 1 continued

Earthquake date and time (UTC)	Epicentral area (country, number of records)	SOF	Depth (km)	M_W	Reference for fault plane solution or R_{RUP} values
2000_July_02_20:03	Near Miyakejima Island (J, 16)	N	18[d]	5.6[b]	–
2000_July_23_21:52	Near Niijima Island (J, 7)	N	9[d]	5.6[b]	–
2000_July_27_01:49	Near Miyakejima Island (J, 7)	SS	12[d]	5.5[b]	–
2000_July_30_00:18	Near Miyakejima Island (J, 4)	SS	14[d]	5.7[b]	–
2000_July_30_12:49	Near Miyakejima Island (J, 6)	SS	18[d]	5.6[b]	–
2000_August_03_13:18	Near Niijima Island (J, 7)	N	12[d]	5.2[b]	–
2000_August_18_01:52	Near Niijima Island (J, 7)	SS	11[d]	5.7[b]	–
2000_September_03_08:36	Yountville (C, 3)	SS	9.4[e]	5[e]	–
2000_October_06_04:30	W Tottori Prefecture (J, 42)	SS	11[d]	6.6[b]	Cauzzi et al. (2008)
2000_October_08_04:17	Shimane Hiroshima Border (J, 53)	SS	8[d]	5.1[b]	–
2002_April_28_13:23	NW Off Ishigakijima Island (J, 1)	N	16[d]	5[b]	–
2002_January_12_00:18	NW Off Miyakojima Island (J, 1)	N	5[f]	5.2[b]	–
2002_June_22_02:58	Changureh–Avaj (I, 35)	R	15[b]	6.5[b]	Ghasemi et al. (2006)
2002_November_03_22:12	Denali Fault (A, 4)	SS	4.9[m]	7.9[m]	COSMOS databank
2003_May_01_00:27	Bingol (T, 1)	SS	10[a]	6.3[b,a]	Milkereit et al. (2004)
2003_July_25_15:13	N Miyagi Prefecture (J, 15)	R	12[d]	5.5[b]	–
2003_July_25_22:13	N Miyagi Prefecture (J, 47)	R	12[d]	6.1[b]	Nishimura et al. (2003)
2003_July_26_07:56	N Miyagi Prefecture (J, 46)	R	12[d]	5.3[b]	–
2003_December_22_19:15	San Simeon (C, 2)	R	7.6[e]	6.4[e]	Graizer and Dreger (2004)
2003_December_26_01:56	Bam (I, 1)	SS	15[b]	6.6[b]	Ghasemi et al. (2008)
2004_September_28_10:15	Parkfield (C, 30)	SS	7.9[g]	6[g]	CESMD
2004_October_23_08:56	Mid Niigata Prefecture (J, 46)	R	13[d]	6.6[f]	Cauzzi et al. (2008)
2004_October_23_09:34	Mid Niigata Prefecture (J, 43)	R	14[d]	6.3[f]	Iio et al. (2009)
2004_October_27_01:40	Mid Niigata Prefecture (J, 49)	R	12[d]	5.8[f]	Geographical Survey Institute
2004_November_09_18:43	Mid Niigata Prefecture (J, 22)	R	5[d]	5.1[f]	–
2004_December_14_05:56	Rumoi (J, 29)	R	9[d]	5.7[f]	Geographical Survey Institute
2005_February_22_02:25	Zarand (I, 12)	R	12[b]	6.4[b]	Nicknam et al. (2007)
2005_March_20_01:53	NW Off Kyushu (J, 37)	SS	9[d]	6.6[f]	Cauzzi et al. (2008)
2005_March_22_06:55	NW Off Kyushu (J, 2)	SS	11[d]	5[f]	–
2005_April_19_21:11	NE Fukuoka Prefecture (J, 65)	SS	14[d]	5.4[f]	–
2005_June_12_15:41	Anza (C, 8)	SS	14.1[e]	5.2[e]	–
2005_June_20_13:03	Mid Niigata Prefecture (J, 43)	R	15[d]	4.9[d]	–

Table 1 continued

Earthquake date and time (UTC)	Epicentral area (country, number of records)	SOF	Depth (km)	M_W	Reference for fault plane solution or R_{RUP} values
2005_September_08_11:27	Vallorcine (CH, 4)	SS	8[e]	4.5[o]	–
2007_April_15_03:19	N Mie Prefecture (J, 14)	R	16[d]	5[f]	–
2007_March_25_00:42	Off Noto Peninsula (J, 48)	R	11[d]	6.7[f]	Cauzzi et al. (2008)
2007_March_25_09:11	Noto Peninsula (J, 35)	R	13[d]	5.2[f]	–
2007_June_10_18:45	Off Noto Peninsula (J, 39)	R	7[d]	4.8[f]	–
2007_June_21_18:34	NW Off Hokuriku District (J, 31)	R	8[d]	4.5[f]	–
2007_July_16_01:13	Off S Niigata Prefecture (J, 14)	R	17[d]	6.6[f]	Tabuchi et al. (2008)
2007_September_30_17:21	Hakone Region (J, 71)	R	14[d]	4.7[f]	–
2008_January_25_19:33	Noto Peninsula (J, 39)	R	11[d]	4.6[f]	–
2008_May_12_06:28	Sichuan (CN, 16)	R	19[e]	7.9[e]	Personal communication to the authors
2008_May_29_15:45	Olfus (IC, 4)	SS	9[e]	6.3[e]	Icelandic Met Office
2008_June_13_23:43	Southern Iwate Prefecture (J, 80)	R	7.8[e]	6.9[f]	Cauzzi et al. (2008)
2008_June_14_00:20	Southern Iwate Prefecture (J, 42)	R	6[d]	5.5[f]	–
2009_April_06_01:32	L'Aquila (IT, 3)	N	8.3[h]	6.3[h]	Gallovič and Zahradník (2012)
2009_April_06_02:37	L'Aquila (IT, 2)	N	8.7[h]	5.1[h]	ITACA
2009_May_12_10:40	Mid Niigata Prefecture (J, 21)	R	12[d]	4.6[f]	–
2009_August_10_20:07	S Suruga Bay (J, 9)	R	23[d]	6.2[f]	Geographical Survey Institute
2009_December_17_23:45	E Off Izu Peninsula (J, 43)	SS	5[d]	4.9[f]	–
2010_September_3_16:35	Darfield (NZ, 38)	R	5[g]	7.1[k]	CESMD
2011_February_21_23:51	Christchurch (NZ, 8)	SS	5[l]	6.3[k]	GNS
2011_February_22_00:04	Christchurch (NZ, 6)	SS	5.9[e]	5.5[e]	USGS
2011_June_13 _02:20	Christchurch (NZ, 8)	SS	7[l]	6[l]	GNS
2011_June_5_21:09	Christchurch (NZ, 1)	SS	9[l]	5.1[l]	GNS
2011_September_29_19:05	E OFF Fukushima Pref. (J, 1)	N	9[j]	5.4[j]	NIED
2012_May_20_03:02	Emilia (IT, 1)	R	10[h]	5.1[h]	ITACA
2012_May_29_07:00	Emilia (IT, 12)	R	10.2[h]	6[h]	Atzori et al. (2012), Pezzo et al. (2013)
2012_May_29_08:25	Emilia (IT, 3)	R	3.2[h]	4.7[h]	ITACA
2012_May_29_08:27	Emilia (IT, 5)	R	10[h]	4.91[h]	ITACA
2012_May_29_10:55	Emilia (IT, 5)	R	6.8[h]	5.5[h]	ITACA
2012_May_20_17:37	Emilia (IT, 1)	R	3.2[h]	4.5[h]	ITACA

Table 1 continued

Earthquake date and time (UTC)	Epicentral area (country, number of records)	SOF	Depth (km)	M_W	Reference for fault plane solution or R_{RUP} values
2012_June_03_19:20	Emilia (IT, 7)	R	9.2[h]	4.9[h]	ITACA
2014_March_28_21:09	La Habra (C, 13)	R	4.8[g]	5.1[g]	CESMD

Geographical origin of data shown in the second column: Italy (IT), Japan (J), Iceland (IC), Iran (I), Turkey (T), California (C), Alaska (A), China (CN), Switzerland (CH), Greece (GR) and New Zealand (NZ). Column 3 lists the style-of-faulting (SOF): normal (N), reverse (R) and strike-slip (SS)

[a] ESMD (http://www.isesd.hi.is/ESD_Local/frameset.htm)
[b] Harvard Global CMT (http://www.globalcmt.org/CMTsearch.html)
[c] ESG98
[d] K-Net (http://www.kyoshin.bosai.go.jp/)
[e] USGS (http://www.usgs.gov/)
[f] F-Net (http://www.fnet.bosai.go.jp)
[g] CESMD (http://www.strongmotioncenter.org/)
[h] ITACA (http://itaca.mi.ingv.it)
[i] Icelandic Strong-Motion Network (http://jardskjalftamidstod.hi.is/en/icelandic_strong_motion_network)
[j] Kik-Net (http://www.kyoshin.bosai.go.jp/)
[k] Syracuse et al. (2013)
[l] GNS (http://www.gns.cri.nz/)
[m] COSMOS (http://www.cosmos-eq.org/)
[n] Zeng and Chen (2001)
[o] Deichmann et al. (2006)
[p] Here and elsewhere, reference not given as $M_W \leq 5.7$

Table 2 Distribution of earthquakes and records in the dataset by geographical origin, style-of-faulting (N = normal, R = reverse; SS = strike-slip) and magnitude

Geographical origin	Style of faulting # events (# records)	M_W range
Japan	N: 7 (43)	5–5.7
	R: 22 (803)	4.5–6.9
	SS: 20 (602)	4.9–6.9
Pan-European region	13 (49)	4.5–6.9
	9 (81)	4.5–6.5
	13 (65)	4.5–7.6
Western USA	0	
	2 (15)	5.1–6.4
	5 (64)	5–7.9
New Zealand	0	
	1 (38)	7.1
	4 (23)	5.1–6.3
China and Taiwan	0	
	2 (95)	7.6–7.9
	0	

Unlike Cauzzi and Faccioli (2008), we did not carry out a refined investigation on the possible regional dependence of peak-motions and response spectra in the dataset, as it is nowadays largely accepted to merge earthquake data from different seismic provinces

Table 3 Distribution of records in the dataset by magnitude, distance and ground types

R_{RUP} (km)\M_W	≤5	5–5.5	5.5–6	6–6.5	6.5–7	7–7.5	7.5–8
<20	A: 10	6	3	9	4	1	1
	B: 8	13	25	14	11	2	23
	C: 21	31	40	16	11	12	7
	D: 2	2	2	2	1	0	0
20–40	7	3	4	7	2	0	0
	18	28	18	18	18	4	8
	16	22	23	16	14	17	12
	9	8	2	6	8	1	0
40–60	1	2	0	4	2	0	2
	22	27	26	17	23	5	7
	16	25	15	14	15	2	9
	9	7	3	3	13	0	2
60–80	1	2	0	2	0	0	0
	27	29	28	17	20	3	5
	18	22	25	18	16	2	9
	9	7	2	3	3	0	0
80–100	0	3	2	1	1	1	0
	31	39	12	17	33	7	3
	18	18	28	19	14	3	15
	8	4	2	3	4	0	1
100–120	1	1	1	2	2	0	0
	25	23	13	19	26	1	0
	13	11	12	13	15	2	4
	3	11	4	3	3	0	1
>120	1	3	0	0	0	0	0
	21	40	20	23	28	1	1
	17	28	24	17	17	4	2
	9	7	4	6	5	0	0

provided the general tectonic context (e.g. active shallow crustal seismicity) is the same (e.g. Ancheta et al. 2014). The effect of regionalisation on the predictive models was found by Boore et al. (2014) to significantly influence only the anelastic attenuation with distance, not taken into consideration in our study.

Finally, we do not dwell herein upon the appropriateness of the logarithmic transformation of independent variables in our prediction model. The reader is referred to Cauzzi and Faccioli (2008), Yamada et al. (2009), Paolucci et al. (2011) and Yamada et al. (2011) for a comprehensive discussion about this topic.

3 Functional forms

Aimed at a simple though physically sound interpretation of the available data, the following predictive model was chosen:

$$\log_{10} y = f_M + f_R + f_S + f_{SOF} + \varepsilon \tag{2}$$

where

$$f_M = c_1 + m_1 M_W + m_2 M_W^2, \tag{3}$$

$$f_R = (r_1 + r_2 M_W) \log_{10}(R_{RUP} + r_3), \tag{4}$$

$$f_S = s_B S_B + s_C S_C + s_D S_D, \text{ or alternatively} \tag{5}$$

$$f_S = b_V \log_{10}\left(\frac{V_{S,30}}{V_A}\right), \text{ or alternatively} \tag{6}$$

$$f_S = b_{V800} \log_{10}\left(\frac{V_{S,30}}{800}\right), \tag{7}$$

$$f_{SOF} = f_N F_N + f_R F_R + f_{SS} F_{SS}. \tag{8}$$

y can be either the 5 %-damped displacement response spectrum $DRS\,(T; 5\,\%)$ in cm or peak ground acceleration PGA ($\mathrm{cm\,s^{-2}}$) or peak ground velocity PGV ($\mathrm{cm\,s^{-1}}$). Prediction of pseudo-spectral acceleration values can be obtained as $PSA\,(T; 5\,\%) = DRS\,(T; 5\,\%) \times (4\pi^2/T^2)$. $PGA \sim PSA\,(0.01\,\mathrm{s}; 5\,\%)$. Consistently with many other ground-motion prediction models in Europe and worldwide (e.g. Douglas et al. 2014), the horizontal seismic action is represented here by the geometric mean (GM) of the DRS ordinates of the two orthogonal horizontal components at a given vibration period T or by the GM of the two orthogonal horizontal PGA and PGV values. c_1, $m_{1,2}$, $r_{1,2,3}$, $s_{B,C,D}$, b_V, b_{V800}, V_A, $f_{N,R,SS}$ are numerical coefficients function of period, to be determined through regressions. ε is a random error term assumed as normally distributed with zero mean and standard deviation $\sigma\,(log_{10} y)$, given by the combination

$$\sigma = \sqrt{\phi^2 + \tau^2} \tag{9}$$

of a within-event component ϕ and a between-event component τ resulting from the regression procedure. Unlike in Cauzzi and Faccioli (2008), explicitly modelled in the present study are: (a) the saturation with magnitude through the term $m_2 M_W^2$, (b) the saturation with distance by using the finite-fault distance R_{RUP} (assumed equal to the hypocentral distance R for $M_W < 5.8$ as explained in the introduction) and the near-source saturation term r_3, (c) a magnitude-dependent geometric attenuation term $(r_1 + r_2 M_W)$, allowing ground-motions and response spectral amplitudes generated by high-energy events to decay slower than those caused by low-magnitude events. A simple period-dependent saturation term r_3 was preferred to a magnitude- and period-dependent one (see Kanno 2006; Faccioli et al. 2010b; Cauzzi et al. 2011) based on the observed stability of the regression results and minimized trade-off of the regression coefficients. Further, and more important, using a saturation term independent of magnitude allows the use of a two-stage regression technique through which the effect of magnitude and distance on observed ground motions can be decoupled (Cauzzi et al. 2008), yielding a smaller standard deviation of the prediction. Similar to Cauzzi and Faccioli (2008), a dissipative attenuation term $r_4 R_{RUP}$ was not included in Eq. (4) due to its negligible impact on ground-motion predictions within the distance range at hand ($R_{RUP} < 150\,\mathrm{km}$).

Three alternative approaches are proposed for predicting site amplification, either based on ground categories (Eq. 5) or on $V_{S,30}$ (Eqs. 6, 7). S_B, S_C, S_D are dummy variables for the main ground categories contemplated in Eurocode 8 (CEN 2004), with the following values: $S_B = S_C = S_D = 0$ for ground type A (rocklike, with $V_{S,30} \geq 800\,\mathrm{m\,s^{-1}}$); $S_B = 1$ and $S_C = S_D = 0$ for ground type B (stiff, with $360\,\mathrm{m\,s^{-1}} \leq V_{S,30} < 800\,\mathrm{m\,s^{-1}}$); $S_B = S_D = 0$, $S_C = 1$ for ground type C (soft, with $180\,\mathrm{m\,s^{-1}} \leq V_{S,30} < 360\,\mathrm{m\,s^{-1}}$) and $S_B = S_C = 0$, $S_D = 1$ for ground type D (very soft, with $V_{S,30} < 180\,\mathrm{m\,s^{-1}}$). $V_{S,30}$ is the travel-time

averaged shear-wave velocity in the uppermost 30 m of the soil column. F_N, F_R, F_{SS} are dummy variables for the main faulting styles (normal, reverse, strike-slip) attributed based on the plunges of the P-, T-, and B-axes, following Boore and Atkinson (2008). F_N, F_R, F_{SS} are equal to 1 for normal, reverse and strike-slip style-of faulting respectively, and equal to zero otherwise. If the style of faulting is unknown, Eq. (2) allows to predict ground-motion and response spectra for unspecified type of focal mechanism by setting $f_{SOF} = 0$. Note however that evaluating the model without style-of-faulting terms actually corresponds to a mechanism that is equal to the weighted average of normal, strike-slip and reverse motions in the dataset (based on the number of records in each class, see Table 2). The reader is referred to Bommer et al. (2003) for a comprehensive discussion about the inclusion of style-of-faulting terms in ground-motion prediction models and seismic hazard assessment.

4 Regression method and procedure

The determination of the period-dependent coefficients of the predictive model required several steps, as described in the following.

(a) Exploratory non-linear regressions using the Matlab® function *lsqcurvefit* were first carried out to investigate the overall variation of the regression coefficients and to identify possible trade-off amongst different terms of the predictive models. From the results of this step we retained $r_2(T)$ and $r_3(T)$, assumed to be known a-priori in the subsequent steps.

(b) Maximum-likelihood (ML) two-stage regressions (Joyner and Boore 1993, 1994) were performed to estimate the attenuation-with-distance coefficient r_1, the site coefficients $s_{B,C,D}$, and the scaling with magnitude (coefficients c_1, m_1 and m_2). This step was repeated twice: the results of the first run were used to carefully inspect $m_2(T)$ and to smooth its variation at short periods ($T < 1$ s) by fitting a high-order polynomial to the raw output of the regressions. The ML two-stage regressions were then repeated assuming $m_2(T)$ known a-priori. As expected, the operation had a positive effect on the stability of $c_1(T < 1\,\text{s})$ and $m_1(T < 1\,\text{s})$ as well.

(c) ML two-stage regressions were run to compute the coefficients of Eqs. (6) and (7), i.e. b_V, b_{V800} and V_A. As in Cauzzi and Faccioli (2008), b_V and V_A are period-dependent coefficients computed *via* a two-stage weighted regression, in which the dependent variables are the residuals (with respect to the motion predicted by Eq. 2 at rock sites) at those stations where $V_{S,30}$ measurements are available. In Eq. (7) the additional constraint $V_A = 800\,\text{m s}^{-1}$ is imposed and therefore only $b_{V800}(T)$ is obtained from the regressions.

(d) ML two-step regression to determine the style-of faulting terms. Following Cauzzi and Faccioli (2008), we retained c_1, m_1 and m_2 from step (b) and solved for the coefficients $f_N, f_R, and\ f_{SS}$ of the fault-type dummy variables. This leads to constraining the scaling of amplitudes with magnitude to be the same for all faulting styles, allowing predictions for unspecified fault types as well as corrections to the average predicted amplitude level according to the fault mechanisms. The coefficients of the predictive equations are available as Online Resource, along with Matlab® scripts for the implementation of Eq. (2).

Note that coefficient r_3, i.e. the saturation with distance, has the physical meaning of the distance to the closest asperity on the fault influencing the response spectral amplitudes at a given period T. Therefore its overall variation, in spite of local perturbation, shows a general

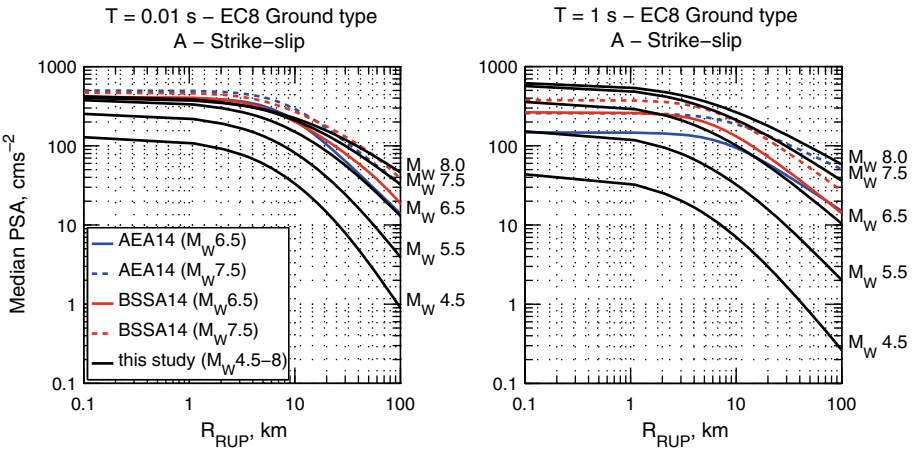

Fig. 3 Comparisons among the median predictions of *PSA* ($T = 0.01$ s) (*LHS*) and *PSA* ($T = 1$ s) (*RHS*) obtained through Eqs. (3) and (4) and the models of Akkar et al. (2014a,b), AEA14, and Boore et al. (2014), BSSA14

decreasing trend with increasing period. As to the linear magnitude scaling m_1, we anticipate here that its variation with period controls the basic shape of the *DRS* and their corner periods, as shown later in this article.

5 Results

5.1 Attenuation with distance

Shown in Fig. 3 are the comparisons between the median predictions of *PSA* ($T = 0.01$ s) (LHS) and *PSA* ($T = 1$ s) (RHS) obtained through Eq. (2) and the recently published models of Akkar et al. (2014b), hereinafter AEA14 (blue curves), and Boore et al. (2014), hereinafter BSSA14 (red curves). *PSA* attenuation is computed for scenario strike-slip events with magnitude between 4.5 and 8 and 0.1 km $\leq R_{RUP} \leq$ 100 km. While the present model is based on R_{RUP}, AEA14 and BSSA14 use the distance from the surface projection of the ruptured fault R_{JB} (Joyner and Boore 1981). For the sake of simplicity, the AEA14 and BSSA14 spectra shown in Fig. 3 were computed for $M_W = 6.5$ and $M_W = 7.5$ only, assuming a causative fault with dip = 90° and rupturing the surface, so that $R_{RUP} = R_{JB}$. AEA14 curves are computed for $V_{S,30} = 800\,\mathrm{m\,s^{-1}}$, while our predictions are for generic rock-like ground type, i.e. based on Eqs. (3) and (4). The red curves in Fig. 3 refer to the BSSA14 predictive model with $V_{S,30} = 800\,\mathrm{m\,s^{-1}}$. The three models show a good agreement in both amplitude and shape at very short periods ($T = 0.01$ s, LHS of Fig. 3)—with our predictions being generally slightly lower at short distances—while large differences are apparent at $T = 1$ s (LHS of Fig. 3), with AEA14 being at least three times lower than BSSA14 and our results for $M_W = 6.5$ and $R_{RUP} < 1$ km. Note however that our predictions change considerably if the site amplification f_S is modelled through Eq. (6) with $V_{S,30} = 800\,\mathrm{m\,s^{-1}}$, as shown in Fig. 4. In this case, the three models are in good agreement for $T = 0.01$ s over the whole distance range (LHS of Fig. 4): for $R_{RUP} > 2$ km the median amplitudes obtained through our predictive model are remarkably consistent with BSSA14, while minor differences w.r.

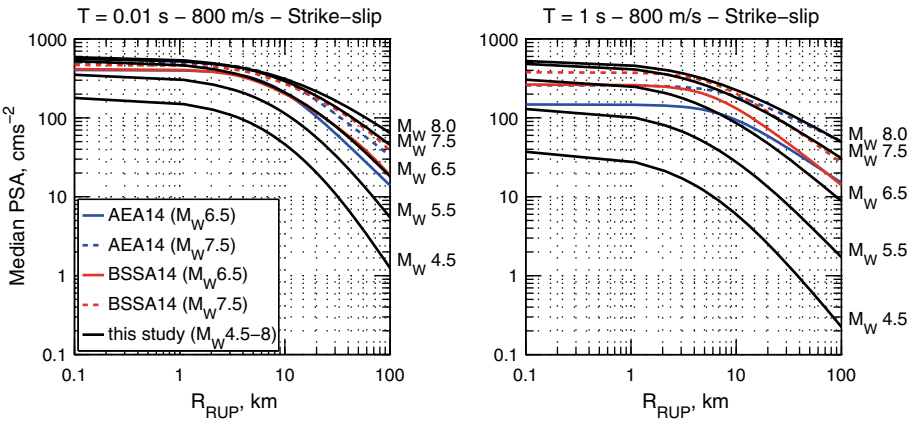

Fig. 4 As Fig. 3, but using Eqs. (3), (4) and (6)

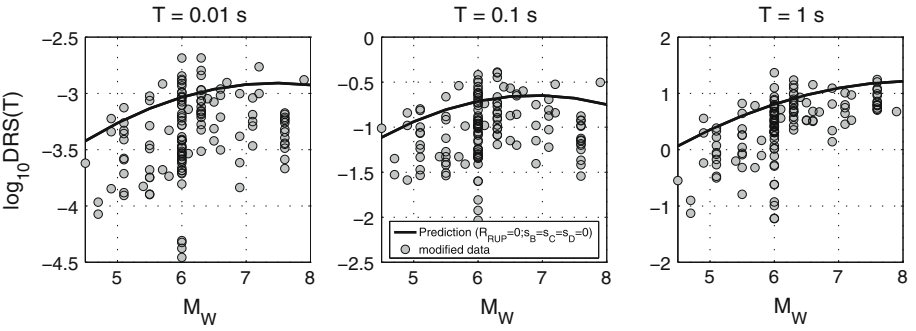

Fig. 5 Comparison between the predicted magnitude scaling at $R_{RUP} = 0$ and the data available for $R_{RUP} < 10$ km. All data were corrected to rock-like ground type, as described in the text. Note the moderate oversaturation with M_W predicted by Eqs. (3) and (4) at short periods

to AEA14 can be appreciated for $R_{RUP} > 10$ km. At $T = 1$ s, our predictive model is in good agreement with BSSA14 for $M_W = 6.5$ at short distances, while for $M_W = 7.5$ the two models have similar shape and amplitudes over the whole distance range (RHS of Fig. 4). As in Fig. 3, AEA14 predicts the lowest *PSA* values at intermediate periods for both magnitude values. This behaviour most likely derives from the data selection and processing (low-pass filtering) applied by the authors to the waveforms available in the *RESORCE* dataset. The impact of such choices on spectral predictions at intermediate and long periods will become more apparent in Sect. 5.4.

5.2 Magnitude scaling and oversaturation

The magnitude scaling of the predictive model for three selected spectral ordinates is shown as black curves in Fig. 5, obtained by evaluating Eqs. (3) and (4) at $R_{RUP} = 0$ km. As apparent from the picture, the predicted spectral amplitudes over-saturate at short periods ($T < 0.2$ s), i.e. for moment magnitude values exceeding $M_{Wsat}(T)$, the predicted spectral levels tend to decrease with increasing M_W (see also Boore et al. 2014). $M_{Wsat}(T)$ is minimum and equal to 6.8 for $0.02 < T < 0.2$ s. The predicted behaviour is shown together with the available

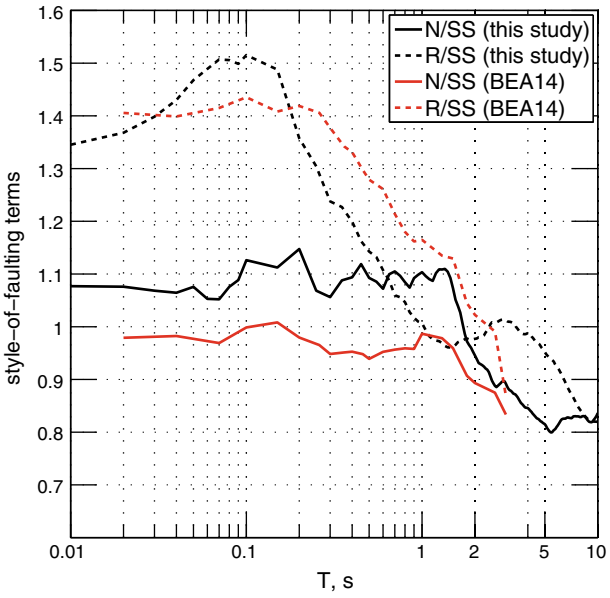

Fig. 6 Style-of-faulting terms $f_{N,R,SS}$ as obtained in this study compared to those computed by Bindi et al. (2014), BEA14

near-source data (for $R_{RUP} < 10$ km) corrected to rock-like ground conditions by subtracting the f_S terms of Eq. (5) from the response spectra. As apparent from Fig. 5, oversaturation with magnitude, where predicted by the regression model, is moderately supported by the available data, although the scarcity of near-field recordings for $M_W > 7.2$ gives rise to large epistemic uncertainties as to the modelling of this near-source feature. This is most likely physically driven by the attenuation of the high-frequency components of ground-motions generated by local asperities over the large distances corresponding to the fault planes of high-energy events. Similar to Boore et al. (2014), we retain the effect of oversaturation in our predictive model. However, we suggest to the interested users a simple recipe to remove oversaturation a-posteriori from the predictions. For the spectral periods showing oversaturation, the suggested approach is based on the computation of $y_0 = 10^{Eq.(2)|_{R_{RUP}=0}}$ and $y_{SAT,0} = 10^{Eq.(2)|_{M_W=M_{W\,sat}\,\&\,R_{RUP}=0}}$. The actual (oversaturating) prediction $y = 10^{Eq.(2)}$ is subsequently scaled as:

$$y_{NO\_OS} = y\frac{y_{SAT,0}}{y_0} \tag{10}$$

where y_{NO_OS} is the modified prediction avoiding oversaturation. Equation (10) prescribes perfect saturation at $R_{RUP} = 0$, while preserving the physically sound magnitude-dependent geometrical decay of the predictive equations. Equation (10) is available as an option in the sample Matlab® implementation of Eq. (2), given as Electronic Supplementary Material.

5.3 Effect of style-of-faulting

The effect of the earthquake faulting style on the ground motion predictions is shown in Fig. 6, in which the corrective terms for normal and reverse style-of-faulting (SOF) are normalized with respect to the strike-slip term of Eq. (8). The present results are compared to

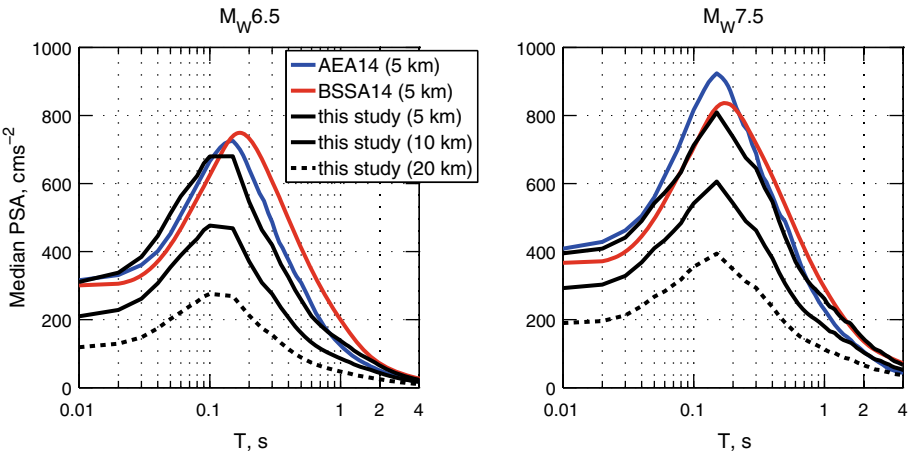

Fig. 7 Comparisons in terms of median *PSA* spectra at rock sites among the predictive equations derived in this study (Eqs. 3, 4, 6) and those of Akkar et al. (2014a, b), AEA14 and Boore et al. (2014), BSSA14

those of Bindi et al. (2014), BEA14, using their regression model with hypocentral distance and EC8-ground types. While notably consistent with BEA14, although slightly different in amplitude, the spectral amplitudes obtained through Eq. (8) for reverse-fault events are systematically higher than the strike-slip predictions for $T < 1$ s, and exhibit a broad peak for $0.02 < T < 0.2$ s. Conversely, at longer periods, the predicted spectral amplitudes are larger for strike-slip faulting. This trend seems to be captured by AEA14 as well, although its predictions do not exceed 3 s period. As to the corrections for normal SOF, our model shows a moderate amplification for $T < 1.5$ s, with shape similar to BEA14. At longer periods the predictions for normal SOF are largely de-amplified w.r. to strike-slip scenarios.

5.4 Response spectra at rock sites

Figure 7 shows the median *PSA* spectra at rock sites yielded by the present predictive equations, with those of Akkar et al. (2014b) and of Boore et al. (2014). Similar to the previous section, we considered strike-slip event scenarios with $M_W = 6.5$ (LHS of Fig. 7) and $M_W = 7.5$ (RHS) with vertical fault planes rupturing the surface, so that $R_{RUP} = R_{JB}$. Equations (3), (4) and (6) are used with $V_{S,30} = 800\,\mathrm{m\,s^{-1}}$ and R_{RUP} equal to 5 km (black thick solid curves), 10 km (black solid curves) and 20 km (black dashed curves). $V_{S,30}$ is equal to $800\,\mathrm{m\,s^{-1}}$ for Akkar et al. (2014b) and Boore et al. (2014). The former (blue thick curves) and the latter (red thick curves) models are only applied for $R_{RUP} = R_{JB} = 5$ km, to emphasise the different features of the predictive tools in the very-near-source region. The three models show minor though important differences as to the period range corresponding to the peak of the *PSA* spectra. The peaks of AEA14 and BSSA14 spectra are located at ~0.15 s and at ~0.18 s, respectively, for both magnitude values. Our model, conversely, shows a clear shift of the *PSA* peak from about 0.1–0.15 s when moving from $M_W = 6.5$ to $M_W = 7.5$ (RHS). The three models show a reasonable agreement for $T < 0.15$ s. At intermediate periods, say from 0.3 to 0.8 s for $M_W = 7.5$, the median predictions of our model are similar to AEA14 and they are also in good agreement with BSSA14 for $2\,\mathrm{s} < T < 4\,\mathrm{s}$ for both scenarios. BSSA14 exhibits the highest *PSA* values for $0.2\,\mathrm{s} < T < 1.5\,\mathrm{s}$.

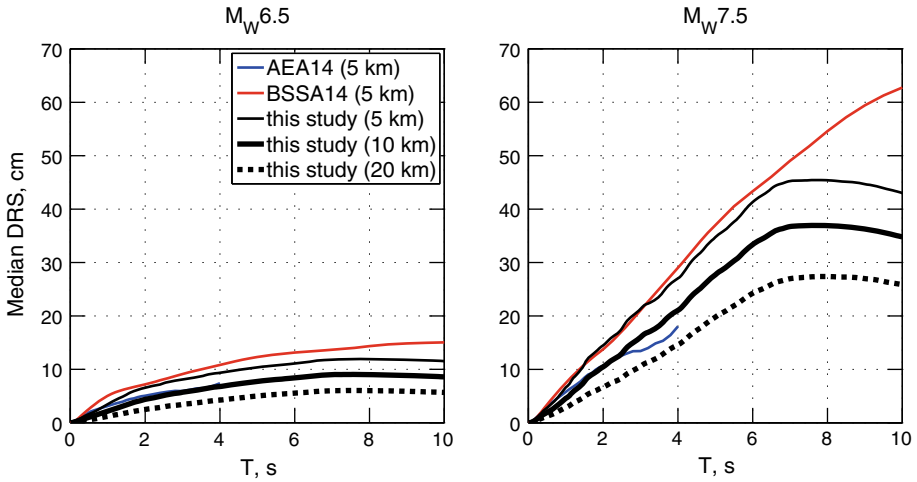

Fig. 8 Comparisons in terms of median *DRS* spectra at rock sites among the predictive equations derived in this study (Eqs. 3, 4, 6) and those of AEA14 and BSSA14

Amongst the three predictive models, AEA14 exhibits the lowest *PSA* amplitudes at $T > 1$ s. This feature is emphasised in Fig. 8, where the previous scenarios are represented as median displacement response spectra. The amplitude of the AEA14 *DRS* for $T > 1$ s can hardly be explained on the basis of physical considerations and is most likely caused by the limitations of the European *RESORCE* dataset at long periods. *RESORCE* includes indeed a "large proportion of records from analogue instruments despite the conversion of most European strong-motion networks to digital accelerometers in the past decade" (Akkar et al. 2014b). As a consequence, AEA14 applied individual filtering to each record and, for a given period, retained only the spectra fulfilling the criteria of Akkar and Bommer (2006). Therefore, the number of records in their databank decreased for $T > 1$ s and, at 4 s, only 60 % of the entries in the original database were used for regressions. Bindi et al. (2014), also based on the *RESORCE* dataset, limited their predictions to $T = 3$ s, acknowledging that "the evaluation of GMPEs at periods longer than 3 s requires an increase of the number of large-magnitude events, that can be achieved including also earthquakes occurred outside Europe." Similar to Cauzzi and Faccioli (2008), the *DRS* predicted using Eqs. (3), (4) and (6) exhibit a strongly increasing initial branch up to a magnitude-dependent corner period varying between ~2 and ~7 s followed by a branch that smoothly tends to the maximum ground displacement either with a nearly constant or a decreasing trend. Although at a first glance our model and BSSA14 show comparable general features, the corner period of BSSA14 for $M_W = 6.5$ is at ~1 s and their *DRS* spectrum is still increasing at $T > 8$ s for $M_W = 7.5$. According to Madariaga (1976), the corner frequency f_c of the far-field S-wave spectrum generated by a circular crack growing up to a radius r_c, may range between $0.2\beta/r_c$ and $0.5\beta/r_c$, depending on the rupture velocity and the source-to-site azimuth. If representative values of the shear-wave velocity $\beta = 3{,}300\,\mathrm{m\,s^{-1}}$ and the rupture radius $r_c = 26$ km (for $M_W = 7.5$, Wells and Coppersmith 1994) are assumed, f_c estimates would range between 0.026 and 0.065 Hz, roughly corresponding to corner periods between 15 and 40 s, consistent with the increasing trend of BSSA14 spectrum for $M_W = 7.5$. Note that these f_c values are considerably lower, typically by a factor of two, than Brune's (1970) estimates based on a kinematic approach (Aki and Richards 2009). The corner period at ~7 s apparent

in our spectra for $M_W = 7.5$ is therefore fully consistent with the model of Brune (1970). However, the comparison with theoretical f_c estimates should not be overemphasised, as shown in Fig. 8 are *recorded* near-field 5 %-damped response spectra and not theoretical far-field Fourier spectra. In this perspective, the work by Faccioli et al. (2004, top panel of their Fig. 4) offers the reader the possibility of a direct comparison with recorded data: the shape of the BSSA14 spectrum for $M_W = 7.5$ is remarkably similar to the average of the spectra of the Chi–Chi (Taiwan) earthquake for distances between 0 and 10 km and Eurocode 8 ground types B and C, while the shape of our spectrum is closer to the average spectra recorded on rock-like ground types for the same event and distance range.

5.5 Site effects

Particular attention was paid to the assessment of period-dependent amplification factors due to local site conditions through Eqs. (5), (6) and (7). Equations (6) and (7) allow estimating the site amplification factor as a continuous function of $V_{S,30}$, thus avoiding undesirable *jumps* when moving from one ground category to the next. Shown in Fig. 9 are representative spectral amplification factors derived herein for EC8 ground types B, C and D, compared to those obtained by Bindi et al. (2014) using ground-type dummy variables s_i (i = B, C or D) and the hypocentral distance as predictors. The solid curves represent site amplification modelled *via* Eq. (6) for $V_{S,30}$ values chosen at mid-range of each ground category. For such $V_{S,30}$ values, the amplitude and shape of the amplification functions predicted by Eq. (6) are remarkably consistent with those yielded by Eq. (5), depicted as dashed curves. Quite evident from Fig. 9 are the differences between the present amplification curves and those of Bindi et al. (2014), derived from the European dataset *RESORCE*. For ground categories C and D in particular, the predicted dominant periods of site response are completely different. The Bindi et al. (2014) curves show a peak at ~1–2 s for C sites and at ~2 s for D sites, while our predictions exhibit a maximum at ~0.5 s for C sites and at ~0.8–1 s for D sites. The practical indication of interest that can be derived from Fig. 9 is that the $V_{S,30}$ values in our dataset seem to reflect themselves into credible dominant periods of site response, while for a *RESORCE*-based model, the peak at e.g. 1–2 s for C sites can hardly be explained by the amplification occurring within the uppermost 30 m of the soil column, suggesting the need for a model refinement based on the predominant period T_0 (see e.g. Zhao et al. 2006, Di Alessandro et al. 2012). Indeed, the site amplification of any prediction model reflects the average amplification phenomena occurring through the whole crust and not only in the shallower sediments. Therefore, even if $V_{S,30}$ is used as predictor, the presence of deep soil sites in the reference dataset may result into a shift of the peak site response towards long periods.

Figure 10 shows the variation of the coefficients of Eqs. (6) and (7) as a function of vibration period T, compared to the previous findings of Cauzzi and Faccioli (2008) and the *RESORCE*-based model of Bindi et al. (2014). The latter uses a period-dependent coefficient γ that has the same meaning of our b_V but is obtained from regressions without explicit modelling of the V_A term. Based on Eq. (6), V_A plays the role of a period-dependent reference shear-wave velocity for bedrock, and approaches 600 m s^{-1} at long periods, as in Cauzzi and Faccioli (2008). Therefore, similar to the latter study, we faced the problem of ensuring consistency among the rock site predictions obtained from Eqs. (3), (4) and from Eq. (6), and we achieved this goal by imposing the additional constraint $V_A = 800$ m s^{-1} in Eq. (7). Apparent from Fig. 10 is that the present model confirms the physically sound asymptotic properties of b_V (negative from regressions): at long periods, $|b_V|$ tends to 0.5, as $(V_A/V_{S,30})^{0.5}$ is the theoretical site amplification for very smooth V_S variation in a sedimentary deposit; on the other hand, $|b_V|$

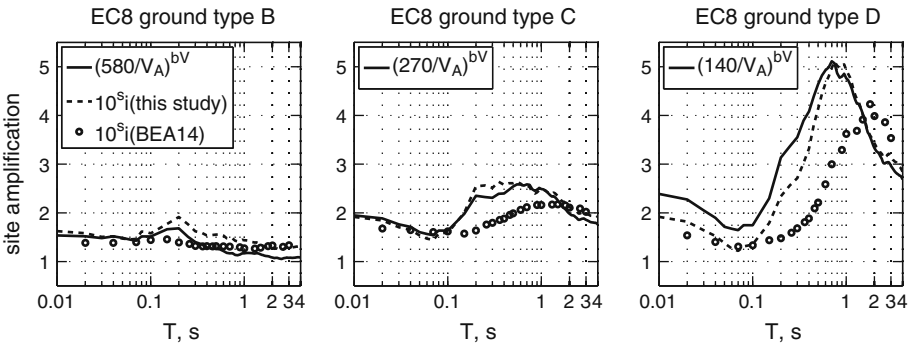

Fig. 9 Site spectral amplification factors for the main ground categories contemplated by the EC8 (CEN 2004) as obtained from Eqs. (5), (6) and (7), compared with the results of Bindi et al. (2014, BEA14). Note how the dataset assembled in the present study allows optimised description of the dominant periods of site response and associated amplification for the different ground types

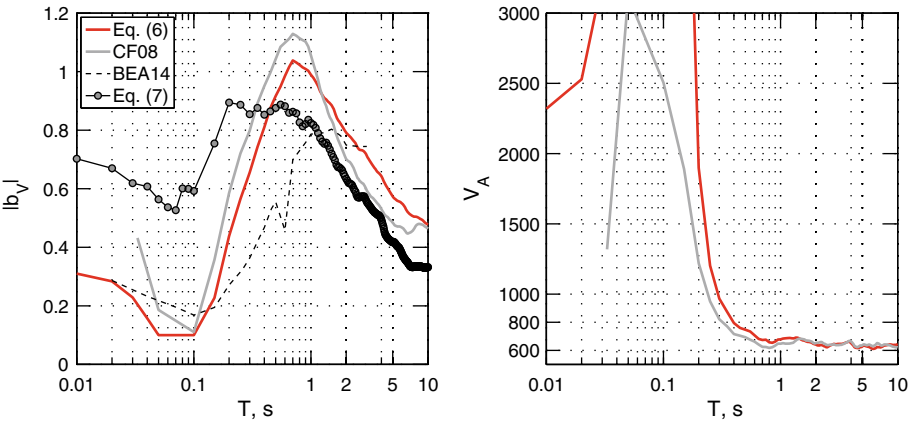

Fig. 10 Site amplification coefficients $|b_V|$ (*LHS*) and V_A (*RHS*) as obtained using Eqs. (6) and (7), compared with the results of Cauzzi and Faccioli (2008, CF08) and Bindi et al. (2014, BEA14). Note the asymptotic properties of b_V explained in the text and the cut-off $b_V < -0.1$ imposed to the regressions to regularize the amplitudes of V_A

reaches 1 in the period range where resonant response of sediments is expected, if the density contrast is neglected. Note from Fig. 10 the cut-off $b_V < -0.1$ imposed to the regressions to regularize the amplitudes of V_A, that would have otherwise diverged for $0.05\,\text{s} < T < 0.1\,\text{s}$.

5.6 Searching for evidence of non-linear soil response in the present dataset

This sub-section illustrates a simple attempt at quantifying potential evidence of non-linear soil behaviour in the dataset at hand. To this aim, we first computed the period-dependent residuals of the predictive model Eqs. (3), (4) and (5) for each GM horizontal spectrum, *PGA* and *PGV* entry i in the database as:

$$res_i(T) = log_{10}\frac{observation(T)_i}{prediction(T)_i}. \tag{11}$$

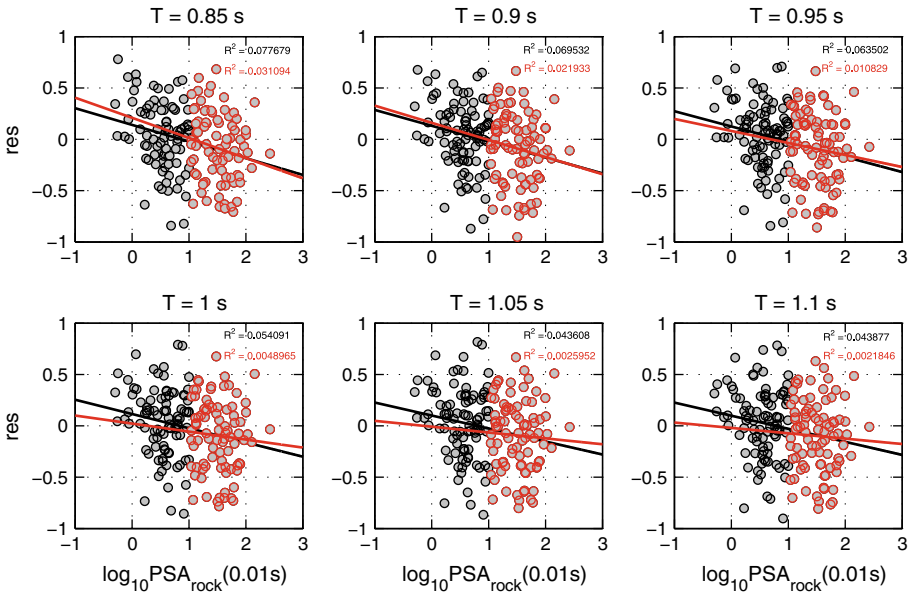

Fig. 11 Ground type D residuals of the predictive model as function of *PSArock (0.01 s)*, computed through Eq. (11) for $0.8\,\text{s} < T < 1.2\,\text{s}$. In each panel, *solid lines* represent the best-fit *straight lines* through the residuals: the *black line* refers to the whole *PSArock* (0.01 s) range while the *red line* is fitted only to data with *PSArock* (0.01 s) $> 10\,\text{cm}\,\text{s}^{-2}$. Note the dramatically low values of the R^2 statistics of the linear regressions

The residuals were then grouped according to the main Eurocode 8 (CEN 2004) ground categories (A, B, C, D) and plotted as a function of the predicted excitation on rock, PSA_{rock} (0.01 s), using Eqs. (3) and (4). The representative set of results for ground type D is shown in Fig. 11 (similar observations were made for ground type C, not reproduced here for the sake of brevity), where emphasis is placed on the few spectral ordinates corresponding to the maximum site amplification $0.8\,\text{s} < T < 1.2\,\text{s}$ (see right panel of Fig. 9). In each panel, the solid lines represent the best-fit straight lines through the residuals: the black line refers to the whole PSA_{rock}(0.01 s) range while the red line is fitted only to data with $PSA_{rock}(0.01\,\text{s}) > 10\,\text{cm}\,\text{s}^{-2}$ (=0.01 g). As apparent from Fig. 11, it is technically possible to fit to the distribution of the residuals decreasing linear trends with increasing PSA_{rock} (0.01 s), that could be interpreted as evidence for apparent non-linearity. However, the largely scattered cloud of points of the residuals does not actually support this modelling assumption, and the R^2 coefficient of the linear fit barely approaches 0.1 when all available data are considered in the regressions, irrespective of the amplitude PSA_{rock} (0.01 s). Similar observations were made at short periods, where soil non-linearity might be expected to be more apparent. We note incidentally that at longer periods, typically for $T > 2\,\text{s}$, the residual clouds of points (not shown here) typically allow linear fitting with positive slope, again associates to dramatically low R^2 statistics. Unlike Sandıkkaya et al. (2013), who re-adjusted the Walling et al. (2008) site amplification model based on the data available in the SHARE databank (Yenier et al. 2010), we believe that the residual plots of Fig. 11—same as the spectral amplification plots of Sandikkaya et al. (2013, their Fig. 6)—are actually too scattered to support a non-linear predictive model. Our present conclusion is consistent with and complements the previous findings of Faccioli et al. (2007) who, working on a subset of the data used in the present study, investigated potential evidence of non-linear soil response by modelling

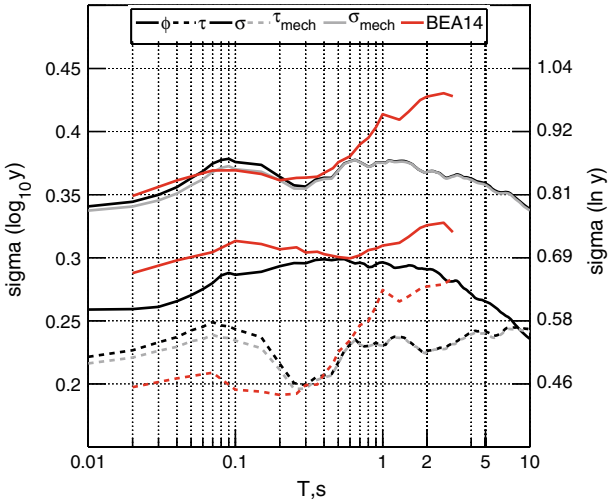

Fig. 12 Total standard deviation of the prediction of Eq. (2) as a function of period T, along with its within-event component ϕ and between-event component τ, compared with the results of Bindi et al. (2014), BEA14. τ_{mech} and σ_{mech} are the between-event component and the total standard deviation of our predictive model if style-of-faulting terms are used. LHS y-axis: $\sigma(\log_{10} y)$. RHS y-axis: $\sigma(\ln y)$

the site terms of Eq. (5) as an exponential function of magnitude but did not observe any significant difference with respect to simple magnitude-independent representation.

5.7 Sigma

Figure 12 shows the total standard deviation of the prediction $\sigma(\log_{10} y)$ and $\sigma(\ln\ y)$ of Eq. (2) as a function of period T, along with its within-event component ϕ and a between-event component τ. The black curves refer to the predictions for unspecified fault mechanism, while the grey curves are associated to the use of style-of-faulting terms. It turned out that the use of Eq. (8) leads to a minor reduction of σ for $T < 0.3$ s. Our estimates are compared to those of Bindi et al. (2014), depicted in Fig. 12 as red curves. As mentioned in the introduction, the total standard deviation obtained herein decreases for $T > 1.5$ s, possibly because of the decrease in scatter induced by site-related amplification effects (see also Cauzzi and Faccioli 2008), while σ of BEA14 starts to increase. The behaviour of the latter is most likely due to "the large variability of the ground-motion at low magnitudes and/or to the low-cut corner filters applied to the small magnitude events […]. The between-events sigma could also be affected by the conversion into M_W from other magnitude scale" in *RESORCE* (Bindi et al. 2014). Similar to Boore et al. (2014), our τ estimates show a peak at ~0.07 s, that might be explained by physical considerations, including a) variations in the source stress parameter (stress-drop) for small magnitude earthquakes (effect not present for larger earthquakes) and b) variations in k_0 for larger magnitude events (Boore et al. 2014). We did not observe any significant difference in ϕ using Eq. (6) or Eq. (7) to describe the amplification due to local site effects, w.r. to the simple parameterisation of Eq. (5). We did not compute the single station standard deviation component ϕ_{ss} of our data, for which global models (eventually dependent on magnitude and distance) are available in the international literature (Rodriguez-Marek et al. 2013).

6 Discussion and conclusions

We have described in this article a new broadband empirically-based predictive model for elastic response spectra, *PGA* and *PGV*, based on a global dataset of high-quality digital acceleration data. The dataset used in this study has been continuously compiled and processed starting from 2007, when the original investigations of Faccioli et al. (2004) on the behavior of displacement spectra at long periods were confirmed by a simple set of prediction equations by Faccioli et al. (2007) and Cauzzi and Faccioli (2008). These earlier studies were motivated by the heightened interest of the engineering community for displacement-based design approaches, requiring long-period seismic input definition (e.g. Priestley et al. 2007; Koketsu and Miyake 2008). As this interest remains high to date, we retained in this study the waveform processing method of Paolucci et al. (2008) and the exclusive use of digital acceleration data, while decreasing the maximum vibration period of the predictions from 20 to $T = 10$ s, that we believe is a reasonable upper bound for engineering applications. A large subset of the present databank was also used as input to standard software tools aimed at providing EC8-compatible acceleration recordings for design in the near-source region of potentially damaging earthquakes (Smerzini et al. 2013).

In spite of its relative success in Europe and worldwide (see Sect. 1) and its clearly stated limits of applicability, the attenuation model of Cauzzi and Faccioli (2008) attracted some criticism due to its simple linear functional form, absence of saturation terms with magnitude and distance, and use of a point-source distance metric (the focal distance). While we note incidentally that point-source distance definitions are nowadays becoming popular again in this domain (Bommer and Akkar 2012; Douglas et al. 2014) due to the ease of implementation in PSHA calculations, we tried in this work to cope with all the aforementioned shortcomings, while keeping with the requirement of simple modelling assumptions aimed at maximum ease of usage of the predictive tool. We adopted therefore a functional form that features magnitude saturation and oversaturation, saturation with distance, use of the rupture distance as predictor, and a geometric attenuation term dependent on magnitude. The same predictive equations are valid over the entire period (0–10 s), magnitude (4.5–8) and distance ($<$150 km) range of the calibration dataset.

Since we did not intend to replicate the results recently obtained from the *NGA-West2*, *SHARE* and *RESORCE* databases, we assembled and processed our data and metadata independently and avoided to adopt exactly the same functional forms used therein. Hence, our updated model does not include elements like the hinge magnitude (see e.g. Boore et al. 2014; Akkar et al. 2014b and Bindi et al. 2014), the fictitious Euclidean distance representation $\sqrt{R_{JB}^2 + h^2}$ (not necessary when the rupture distance is used) and the segregation between linear and non-linear soil response. For the same reason, we did not attempt at developing hanging-wall correction terms or a directivity model, for which results supported by numerical simulation are already available or are being produced by dedicated teams of researchers (see e.g. Donahue and Abrahamson 2014; Spudich et al. 2014). As a result, we believe that our model can effectively contribute to capturing the epistemic uncertainties associated with the prediction of seismic shaking levels for engineering applications. The readers interested in scaling factors for over-damped response spectra over a broad period range can refer to Cauzzi and Faccioli (2008), Faccioli et al. (2010b), Rezaeian et al. (2014) and Akkar et al. (2014c) for a comprehensive discussion on this topic.

Given the large range of vibration periods considered in this study, one potential limitation of the predictive tool is the use of $V_{S,30}$ as proxy for site amplification. However, as noted in Sect. 5.5, we are comforted in this choice by: (a) the fact that the $V_{S,30}$ values in our dataset

seem to reflect themselves into credible dominant periods of site response and, (b) previous studies by Boore (2004) and Boore et al. (2011) showing that $V_{S,30}$ is well correlated to the deeper subsoil structure. While the impact of 2D and 3D basin type effects on and response spectra has been extensively dealt with in the literature by way of analytical tools, its inclusion in empirical ground motion prediction has been mainly operated in a simplified way (e.g. NGA and NGA-West2), through the depth of particular geological formations associated with representative high values of V_S. This was largely limited to California, where the depth in question could be estimated for a number of accelerometer sites; the lack of this type of information still precludes the inclusion of basin-related parameters in attenuation models derived from global databases.

In spite of the large contribution of near-source data to the present dataset, the need for improving the magnitude-distance distribution of recordings on rock-like ground type is still apparent (Fig. 2). Some data will naturally become available in the next few years, but the largest injection will most likely be represented in the near future by the results of deterministic physics-based numerical simulations (e.g. Graves et al. 2011), eventually coupled with semi-stochastic ones (e.g. Edwards and Fah 2013; Bora et al. 2014). Such hybrid models based on both recorded and simulated ground motions will constitute the next generation predictive tools for peak ground motion and response spectra.

Acknowledgments All the sources of our data and metadata are gratefully acknowledged, along with the many people (in particular Roberto Paolucci, Raffaele Figini and Manuela Villani) who partially contributed to the development of this work within the last years. The work presented in this paper was partly motivated by the ongoing SeIsmic Ground Motion Assessment (SIGMA) Project. We are thankful to John Douglas and two anonymous colleagues for reviewing the original manuscript and for providing useful suggestions for improvements.

References

Aki K, Richards PG (2009) Quantitative seismology, 2nd edn. University Science Books, Sausalito

Akkar S, Bommer JJ (2006) Influence of long-period filter cut-off on elastic spectral displacements. Earthq Eng Struct Dyn 35:1145–1165. doi:10.1002/eqe.577

Akkar S, Sandıkkaya MA, Şenyurt M et al (2014a) Reference database for seismic ground-motion in Europe (RESORCE). Bull Earthq Eng 12:311–339. doi:10.1007/s10518-013-9506-8

Akkar S, Sandıkkaya MA, Bommer JJ (2014b) Empirical ground-motion models for point- and extended-source crustal earthquake scenarios in Europe and the Middle East. Bull Earthq Eng 12:359–387. doi:10.1007/s10518-013-9461-4

Akkar S, Sandıkkaya MA, Ay BÖ (2014c) Compatible ground-motion prediction equations for damping scaling factors and vertical-to-horizontal spectral amplitude ratios for the broader Europe region. Bull Earthq Eng 12:517–547. doi:10.1007/s10518-013-9537-1

Ancheta TD, Darragh RB, Stewart JP et al (2014) NGA-West 2 database. Earthq Spectra 140514111412006. doi:10.1193/070913EQS197M

Atzori S, Merryman Boncori JP, Pezzo G, Tolomei C, Salvi S (2012) Secondo report analisi dati SAR e modellazione della sorgente del terremoto dell'Emilia. www.mi.ingv.it

Bindi D, Massa M, Luzi L et al (2014) Pan-European ground-motion prediction equations for the average horizontal component of PGA, PGV, and 5 %-damped PSA at spectral periods up to 3.0 s using the RESORCE dataset. Bull Earthq Eng 12:391–430. doi:10.1007/s10518-013-9525-5

Bommer JJ, Akkar S (2012) Consistent source-to-site distance metrics in ground-motion prediction equations and seismic source models for PSHA. Earthq Spectra 28:1–15

Bommer JJ, Douglas J, Strasser FO (2003) Style-of-faulting in ground-motion prediction equations. Bull Earthq Eng 1:171–203. doi:10.1023/A:1026323123154

Boore DM (2004) Estimating s(30) (or NEHRP site classes) from shallow velocity models (depths <30 m). Bull Seismol Soc Am 94:591–597. doi:10.1785/0120030105

Boore DM, Atkinson GM (2008) Ground-motion prediction equations for the average horizontal component of PGA, PGV, and 5 %-damped PSA at spectral periods between 0.01 s and 10.0 s. Earthq Spectra 24:99. doi:10.1193/1.2830434

Boore DM, Thompson EM, Cadet H (2011) Regional correlations of VS30 and velocities sveraged over depths less than and greater than 30 meters. Bull Seismol Soc Am 101:3046–3059. doi:10.1785/0120110071

Boore DM, Stewart JP, Seyhan E, Atkinson GM (2014) NGA-West 2 equations for predicting PGA, PGV, and 5 %-Damped PSA for shallow crustal earthquakes. Earthq Spectra 131108093828003. doi:10.1193/070113EQS184M

Bora SS, Scherbaum F, Kuehn N, Stafford P (2014) Fourier spectral- and duration models for the generation of response spectra adjustable to different source-, propagation-, and site conditions. Bull Earthq Eng 12:467–493. doi:10.1007/s10518-013-9482-z

Bormann P (ed) (2012) New manual of seismological observatory practice (NMSOP-2), IASPEI, GFZ German Research Centre for Geosciences, Potsdam. http://nmsop.gfz-potsdam.de. doi:10.2312/GFZ.NMSOP-2

Brune JN (1970) Tectonic stress and the spectra of seismic shear waves from earthquakes. J Geophys Res 75:4997–5009. doi:10.1029/JB075i026p04997

Cauzzi (2008) Broadband empirical prediction of displacement response spectra based on worldwide digital records. Ph.D. thesis. Politecnico di Milano

Cauzzi C, Clinton J (2013) A high- and low-noise model for high-quality strong-motion accelerometer stations. Earthq Spectra 29:85–102. doi:10.1193/1.4000107

Cauzzi C, Faccioli E (2008) Broadband (0.05 to 20 s) prediction of displacement response spectra based on worldwide digital records. J Seismol 12:453–475. doi:10.1007/s10950-008-9098-y

Cauzzi C, Faccioli E, Paolucci R, Villani M (2008) Long-period ground motion evaluation from a large worldwide digital strong motion database. In: Proceedings of the 14th WCEE, Beijing, China, paper S10–047

Cauzzi C, Faccioli E, Poggi V, Faeh D, Edwards B (2011) Prediction of long-period displacement response spectra for low-to-moderate seismicity regions. Merging the Swiss waveform archive with a global fully digital strong-motion dataset. In: Proceedings of the ESG4, UCSB

Comité Européen de Normalisation (CEN) (2004). Eurocode 8, Design of structures for earthquake resistance—part 1: general rules, seismic actions and rules for buildings. European Standard NF EN 1998-1, Brussels

Deichmann N, Baer M, Braunmiller J et al (2006) Earthquakes in Switzerland and surrounding regions during 2005. Eclogae Geol Helv 99:443–452. doi:10.1007/s00015-006-1201-1

Delavaud E, Cotton F, Akkar S et al (2012) Toward a ground-motion logic tree for probabilistic seismic hazard assessment in Europe. J Seismol 16:451–473. doi:10.1007/s10950-012-9281-z

Di Alessandro C, Bonilla LF, Boore DM et al (2012) Predominant-period site classification for response spectra prediction equations in Italy. Bull Seismol Soc Am 102:680–695. doi:10.1785/0120110084

Donahue J, Abrahamson N (2014) Simulation-based hanging-wall effects. Earthq Spectra 140609063716004: doi:10.1193/071113EQS200M

Douglas J, Akkar S, Ameri G et al (2014) Comparisons among the five ground-motion models developed using RESORCE for the prediction of response spectral accelerations due to earthquakes in Europe and the Middle East. Bull Earthq Eng 12:341–358. doi:10.1007/s10518-013-9522-8

Edwards B, Fah D (2013) A stochastic ground-motion model for Switzerland. Bull Seismol Soc Am 103:78–98. doi:10.1785/0120110331

Faccioli E, Paolucci R, Rey J (2004) Displacement spectra for long periods. Earthq Spectra 20:347–376. doi:10.1193/1.1707022

Faccioli E, Cauzzi C, Paolucci R et al (2007) Long period strong ground motion and its use as input to displacement based design. In: Pitilakis K (ed) Earthquake geotechnical engineering, 4th international conference on earthquake geotechnical engineering-invited lectures, Springer, pp 23–51. doi:10.1007/978-1-4020-5893-6

Faccioli E, Villani M, Vanini M, Cauzzi C et al (2010a) Mapping seismic hazard for the needs ofdisplacement-based design: The case of Italy. In: Fardis MN (ed) Advances in performance-based earthquake engineering, vol 13. Dordrecht: Springer Netherlands, pp 3–14. doi:10.1007/978-90-481-8746-1

Faccioli E, Bianchini A, Villani M (2010b) New ground motion prediction equations for T > 1s and their influence on seismic hazard assessment. In: Koketsu K (ed) Proceedings of the University of Tokyo symposium on long-period ground motion and urban disaster mitigation, Mar 17–18, 2010, Tokyo, Japan

Fukushima Y, Tanaka T (1990) A new attenuation relation for peak horizontal acceleration of strong earthquake ground motion in Japan. Bull Seismol Soc Am 80:757–783

Gallovič F, Zahradník J (2012) Complexity of the Mw 6.3 2009 L'Aquila (central Italy) earthquake: 1. multiple finite-extent source inversion. J Geophys Res 117:B04307. doi:10.1029/2011JB008709

Ghasemi H, Kamalian N, Hamzeloo H (2006) Stochastic finite-fault simulation for the 2002 Changureh-Avaj earthquake, NW Iran. J Earth Space Phys 32:25–35
Ghasemi H, Zare M, Fukushima Y (2008) Ranking of several ground-motion models for seismic hazard analysis in Iran. J Geophys Eng 5:301–310
Graizer V, Dreger D (2004) Seismological implications of the ground motion data from the 2003 San Simeon earthquake. In: SMIP04 seminar proceedings
Graves RW, Aagaard BT, Hudnut KW (2011) The shakeout earthquake source and ground motion simulations. Earthq Spectra 27:273–291. doi:10.1193/1.3570677
Horikawa H (2001) Earthquake doublet in Kagoshima, Japan: rupture of asperities in a stress shadow. Bull Seismol Soc Am 91:112–127
Ide S (1999) Source process of the 1997 Yamaguchi, Japan, earthquake analyzed in different frequency bands. Geophys Res Lett 26:1973–1976
Iio Y, Shibutania T, Matsumotob S et al (2009) Precise aftershock distribution of the 2004 Mid-Niigata prefecture earthquake—implication for a very weak region in the lower crust. Phys Earth Planet Inter 172:345–352
Joyner WB, Boore DM (1981) Peak horizontal acceleration and velocity from strong-motion records including records from the 1979 Imperial Valley, California, earthquake. Bull Seismol Soc Am 71:2011–2038
Joyner WB, Boore DM (1993) Methods for regression analysis of strong-motion data. Bull Seismol Soc Am 83:469–487
Joyner WB, Boore DM (1994) Errata: methods for regression analysis of strong-motion data. Bull Seismol Soc Am 84:955–956
Joyner WB, Warrik RE, Fumal TE (1981) The effect of quaternary alluvium on strong ground motion in the Coyote Lake, California, earthquake of 1979. Bull Seismol Soc Am 71:1333–1349
Kanno T (2006) A new attenuation relation for strong ground motion in Japan based on recorded data. Bull Seismol Soc Am 96:879–897. doi:10.1785/0120050138
Koketsu K, Miyake H (2008) A seismological overview of long-period ground motion. J Seismol 12:133–143. doi:10.1007/s10950-007-9080-0
Madariaga R (1976) Dynamics of an expanding circular fault. Bull Seismol Soc Am 66:639–666
Milkereit C, Grosser H, Wang R et al (2004) Implications of the 2003 Bingol Earthquake for the interaction between the North and East Anatolian faults. Bull Seismol Soc Am 94:2400–2406
Nicknam A, Eslamian Y, Bozorgnasab M, Nicknam A, (2007) Modification of seismological parameters of Zarand earthquake (2005 February 22), in central Iran, Using Empirical Green's function method. The 2007 Australian Earthq Eng Soc Int Conf of Earthquake-Engineering, Wollongong, Australia
Nishimura T, Imakiire T, Yarai H et al (2003) A preliminary fault model of the 2003 July 26, M6.4 northern Miyagi earthquake, northeastern Japan, estimated from joint inversion of GPS, leveling, and InSAR data. Earth Planets Space 55:751–757
Paolucci R, Rovelli A, Faccioli E et al (2008) On the reliability of long-period response spectral ordinates from digital accelerograms. Earthq Eng Struct Dyn 37:697–710. doi:10.1002/eqe.781
Paolucci R, Cauzzi C, Faccioli E et al (2011) Comment on "Statistical features of short-period and long-period near-source ground motions" by Masumi Yamada, Anna H. Olsen, and Thomas H. Heaton. Bull Seismol Soc Am 101:915–918. doi:10.1785/0120100092
Pezzo G, Merryman Boncori JP et al (2013) Coseismic deformation and source modeling of the May 2012 Emilia (Northern Italy) earthquakes. Seismol Res Lett 84:645–655. doi:10.1785/0220120171
Priestley MJN, Calvi GM, Kowalsky MJ (2007) Displacement-based seismic design of structures. IUSS, Pavia
Rezaeian S, Bozorgnia Y, Idriss IM et al (2014) Damping scaling factors for elastic response spectra for shallow crustal earthquakes in active tectonic regions: "average" horizontal component. Earthq Spectra 30(2):939–963. doi:10.1193/100512EQS298M
Rodriguez-Marek A, Cotton F, Abrahamson NA et al (2013) A model for single-station standard deviation using data from various tectonic regions. Bull Seismol Soc Am 103:3149–3163. doi:10.1785/0120130030
Sandıkkaya MA, Akkar S, Bard P-Y (2013) A nonlinear site amplification model for the new pan-European ground-motion prediction equations. Bull Seismol Soc Am 103:19–32
Smerzini C, Galasso C, Iervolino I, Paolucci R (2013) Ground motion record selection based on broadband spectral compatibility. Earthq Spectra 140514111412006: doi:10.1193/052312EQS197M
Spudich P, Rowshandel B, Shahi S et al (2014) Comparison of NGA-West2 directivity models. Earthq Spectra 140609063716004. doi:10.1193/080313EQS222M
Syracuse EM, Thurber CH, Rawles CJ et al (2013) High-resolution relocation of aftershocks of the Mw7.1 Darfield, New Zealand, earthquake and implications for fault activity. J Geophys Res Solid Earth 118:1–12

Tabuchi H, Harada T, Ishibashi K (2008) A southeasterly-dipping static fault model of the 2007. Niigata-ken Chuetsu-oki, Japan, earthquake based on crustal movements, tsunamis, aftershock distribution and neotectonics. Kobe University Research Center for Urban Safety and Security—research report, no. 12

Walling M, Silva W, Abrahamson NA (2008) Nonlinear site amplification factors for constraining the NGA models. Earthq Spectra 24:243–255

Wells DL, Coppersmith KJ (1994) New empirical relationships among magnitude, rupture length, rupture width, rupture area, and surface displacement. Bull Seismol Soc Am 84:974–1002

Yamada M, Olsen AH, Heaton TH (2009) Statistical features of short-period and long-period near-source ground motions. Bull Seismol Soc Am 99:3264–3274. doi:10.1785/0120090067

Yamada M, Olsen AH, Heaton TH (2011) Reply to "Comment on 'Statistical features of short-period and long-period near-source ground motions' by Masumi Yamada, Anna H. Olsen, and Thomas H. Heaton" by Roberto Paolucci, Carlo Cauzzi, Ezio Faccioli, Marco Stupazzini, and Manuela Villani. Bull Seismol Soc Am 101:919–924. doi:10.1785/0120100210

Yenier E, Sandıkkaya MA, Akkar S (2010) Report on the fundamental features of the extended strong motion databank prepared for the SHARE project. Deliverable 4.1 of seventh framework programme project seismic hazard harmonization in Europe (SHARE), Ankara

Yoshida S, Seta G, Okubo S, Kobayashi S (1999) Absolute gravity change associated with the March 1997 earthquake swarm in the Izu Peninsula, Japan. Earth Planets Space 51:3–12

Zeng Y, Chen C-H (2001) Fault rupture process of the 20 September 1999 Chi-Chi, Taiwan, Earthquake. Bull Seismol Soc Am 91(5):1088–1098

Zhao JX (2006) Attenuation relations of strong ground motion in Japan using site classification based on predominant period. Bull Seismol Soc Am 96:898–913. doi:10.1785/0120050122